Journal of Energy Storage 72 (2023) 108216

Contents lists available at ScienceDirect

Journal of Energy Storage

journal homepage: www.elsevier.com/locate/est

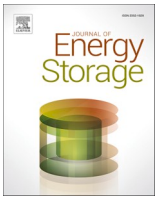

Research papers

# Oxygen-rich functionalized porous carbon by $KMnO_4$ activation on pods of *Prosopis juliflora* for symmetric supercapacitors

K. Vignesh [a,1], M. Ganeshbabu [a,1], N. Prasanna Naga Puneeth [a], T. Mathivanan [a], B. Ramkumar [b], Yun Sung Lee [b], R. Kalai Selvan [a,*]

[a] *Energy Storage and Conversion Devices Laboratory, Department of Physics, Bharathiar University, Coimbatore 641046, Tamil Nadu, India*
[b] *Faculty of Chemical Engineering, Chonnam National University, Gwangju 500-757, South Korea*

ARTICLE INFO

*Keywords:*
*Prosopis juliflora*
Hierarchical porous carbon
$KMnO_4$
Supercapacitor

ABSTRACT

The need for energy storage devices with low-cost electrode material is predominant in joining the race to meet the energy crisis. The present work aims to turn the invasive weed, *Prosopis juliflora* (PJF), to serve energy storage applications under the turning waste into wealth concept. The porous carbon was prepared from PJF at different temperatures (600, 700, and 800 °C) using $KMnO_4$ as the activating agent. The obtained carbon offers oxygen-rich functional groups (36 %), a high specific surface area (1210.4 $m^2g^{-1}$), and a hierarchical porous carbon network. The synthesized carbon (PJF-700) facilitates abundant active sites, which offered a significant energy density of 13.13 Wh $kg^{-1}$ at the power density of 450 W $kg^{-1}$ with an operating voltage window of 1.8 V in 1 M $Na_2SO_4$ electrolyte @ 0.5 A $g^{-1}$. The present work claims its novelty by reporting $KMnO_4$ as the activating agent for *PJF*-derived biomass carbon resulting in oxygen-rich functional groups. The significance of synthesized carbon with distinct properties and promising electrochemical performances for supercapacitors is also explored.

## 1. Introduction

The consumption of excessive fossil fuels, combined with the inevitable dominance of electronic devices, resulted in resource depletion, pollution, and economic imbalance. Therefore, electrochemical energy storage (EES) devices such as metal ion batteries, air batteries [1–3], and supercapacitors are considered the most promising candidates for ensuring a sustainable energy supply. Most importantly, supercapacitors are widely known for their prolonged cycle life and comparatively high power density than batteries. Despite their high-power density, lower energy density is the major drawback of electric double-layer capacitors (EDLCs) [4]. Due to their cost-effectiveness, natural abundance, high porosity, large surface area, and enhanced conductivity, endless carbon-based materials have been used to increase the energy density of supercapacitors. Activated carbon (AC), graphene, graphite, carbide-derived carbons, and carbon aerogels were commonly employed as electric double-layered capacitor (EDLC) materials [5,6]. The EDLC behavior is dependent on the porosity of carbonaceous material, where the micropores (<2 nm) ensure a high specific surface area and the source for storing ions [7], mesopores (2–50 nm) support rapid ionic diffusion [8] and (iii) macropores (>50 nm) enable ion buffer pools for decreasing the distance of ionic diffusion [9,10]. In addition, surface phenomena such as the hydrophilic nature of active material (wettability) and functional groups play an essential role in the adequate performance of EES devices [11]. Therefore, many reports illustrate the importance of hierarchically structured porous carbon synthesized through chemical activation, which provides high specific capacitance and excellent charge/discharge rate [7,8,12]. This is due to the proportionality of characteristic time constant 't', which is directly proportional to the square of diffusion length 'L' ($t \approx L^2/D$) [13,14].

In addition, hetero atoms such as Nitrogen (N) [15], Sulfur (S) [16], Phosphorous (P) [17], Boron (B) [18], Oxygen (O) [19], and Fluorine (F) [20] functionalization have been used to enhance the electrochemical performance owing to the better electronic properties such as conductivity, ionic diffusion, rapid redox reactions, and better electrode wettability. But it involves complex procedures using activating agents to generate porosity and functionalizing agents to produce functional groups on the surface of the porous carbon material [21,22]. Further, these functional groups lead to several drawbacks, including the uneven distribution of N- groups, changing the textural characteristics,

* Corresponding author.
*E-mail address:* selvankram@buc.edu.in (R.K. Selvan).
[1] Both authors have equal contribution

https://doi.org/10.1016/j.est.2023.108216
Received 4 April 2023; Received in revised form 16 June 2023; Accepted 28 June 2023
Available online 8 July 2023

relatively larger atomic size of S may block the micropores, and their poor conductivity may lead to deteriorate the electrochemical performance [23]. However, heteroatom functionalization encompasses time-consuming procedures owing to their multiple-step processes, such as hydrothermal treatment, calcination, activation, functionalization, indefinite acid treatment, and washing procedures. Also, as a significant concern, the above-mentioned functionalization procedures involve highly toxic agents and high temperatures, which leads to the collapse of the pore structure and reduction in surface area.

Recently, it has been identified that the residues of oxygen functional groups without external functionalization helps to increase the capacitive performance. Usually, the presence of oxygen functionalities was always ignored, despite their high contribution to the capacitance in the nitrogen-functionalized activated carbon [24,25]. Also, it has been reported that the electrochemical performance improves while increasing the ratio of oxygen functional groups [19,26]. It is worth emphasizing that the oxygen functional groups (OFG) such as hydroxyl (-OH-), carbonyl (Aldehydes and ketones), and quinone groups increase the electron-rich sites and participate in electron transfer enabling pseudocapacitive contribution in addition to EDLC [27]. It further improves the electrode's wettability and increases the specific surface area. These OFG have been generated using activating agents, including potassium compounds [28] (KOH, $K_2CO_3$, $KHCO_3$, $K_2FeO_4$, and $KNO_3$), sodium hydroxide (NaOH) [29], phosphoric acid ($H_3PO_4$) [30], zinc chloride ($ZnCl_2$) [31], sodium thiosulfate ($Na_2S_2O_3$) [32] and sulfuric acid ($H_2SO_4$) [33]. However, these activators are less likely to produce hierarchical porous carbon, have poor yield, and are primarily hazardous as they are either acidic or eco-toxic. Most importantly, these well-known activators cannot generate potential higher-order OFG on a large scale [34,35].

Exceptionally, few works have been reported using $KMnO_4$ as an activating agent to generate hierarchical porous carbon (HPC) since $KMnO_4$ is an excellent oxidizing agent, environmentally friendly, inexpensive, and water-soluble [36]. This activation process is the easiest method over other known methods such as template methods, non-templating, and incorporating physical activations [37–39]. The pore-generating mechanism and the activation of the carbon precursor are unique, where the activator molecules capture the active sites of the carbon source. Here, the unique characteristic of $KMnO_4$ is that, while reacting with carbon at high temperatures, it produces another activating agent of $K_2CO_3$ [37] . As well as, the Mn compounds get easily oxidized during carbonization and decorated over the carbon matrix, further improving the electrochemical properties [40]. Subsequently, while washing, it creates pore formation. Therefore, $KMnO_4$ acts as a modifier and activator since it can simultaneously produce hierarchical porous nature and oxygen-rich functional groups during carbonization [41].

Given a significant activating agent, choosing the precursor source for carbonization is equally essential. To date, activated carbon has been prepared through different sources such as coal tar, lignite, wood, petroleum pitch, and biomasses [42,43]. However, focusing on precursors having environmental threats and sources with no other valuable by-products is preferrable. One such source is the weed shrub *Prosopis Juliflora (PJF)*. *PJF* is the most intransigent invasive weed [44], widely spread over millions of hectares, and depletes the groundwater, leaving the land useless for agriculture. Therefore, the current work used *PJF* as the carbon precursor and $KMnO_4$ as an activating agent and reported a significant energy density of 13.13 Wh $kg^{-1}$ @ 0.5 A $g^{-1}$ for the fabricated symmetric cell in an aqueous $Na_2SO_4$ electrolyte. Moreover, the previous work involved a two-step calcination procedure, hydrothermal treatment, and pyrolysis; later, acid wash and neutralization eventually resulted in relatively low energy density and poor yield [45]. This work emphasizes the preparation of OFG carbon using one-step pyrolysis technique aimed to obain enhanced energy density. No works have been reported using $KMnO_4$ as an activating agent for *PJF*-based biomass-derived porous carbon synthesis. Thereby, this method of synthesis is unique and highly effective over other porous carbon synthesis procedures.

## 2. Experimental methodology

### 2.1. Preparation of PJF from biomass

Pods of *Prosopis Juliflora (PJF)* collected from the Bharathiar University campus (11.0390 °N, 76.8764 °E) were washed and dried to remove dust impurities. The dried Pod was powdered and sieved using a commercial mesh. The raw powder was mixed with $KMnO_4$ in a weight ratio of 1:1, and the mixture was treated with 200 ml of deionized water and stirred for 12 h at 80 °C [37], where the mixture gets completely dried. During this stirring process, continuous bubbling and expansion of the solution mixture were observed initially. The dried mixture of PJF and $KMnO_4$ was carbonized under a nitrogen ($N_2$) atmosphere at different temperatures (600 °C, 700 °C, 800 °C) with a heating rate of 5 °C/min. After carbonization, the sample was treated with 3 M HCl to remove the insoluble unreacted residues. The acid treated sample is washed with hydrogen peroxide ($H_2O_2$) to make sure that no residues of oxide impurities in the porous regime. The acidic sample was neutralized after several washes with DD water. Then, the activated carbon was dried at 80 °C for 24 h and ground. To differentiate the chemical composition, morphology, and electrochemical characteristics of activated carbon, the samples were labelled as PJF-X, and X indicates the different carbonization temperatures (600 °C, 700 °C, 800 °C). For example, PJF-600 means the *Prosopis Juliflora* derived porous carbon synthesized at 600 °C. Pictorial representation of the synthesis route is shown in Fig. 1.

### 2.2. Preparation of electrodes

The electrodes were prepared using the following methods, The active material PJF-X, carbon black, and polyvinylidene difluoride (PVDF) were mixed in the ratio of 80:15:5 using 0.4 mL of *N*-methyl-2-pyrrolidine (NMP). The mixture was ground well for 2 h to make a well-dispersed homogenous slurry. The obtained slurry was uniformly coated on stainless steel (SS) sheet by drop casting method and dried at 100 °C overnight in the vacuum oven to aid them for electrochemical studies.

### 2.3. Structural characterizations

The physical structure of synthesized PJF at three different temperatures was verified using X-ray diffraction (Model: Rint 1000, Rigaku, Japan) with Cu $K_\alpha$ radiation in the 2θ range of 10° to 80°, and Raman Spectroscopy using HORIBA Jobin Yvon LabRAM HR 800. X-ray photoelectron spectroscopy (XPS) was used to analyze the surface composition using Multilab 2000 (Thermo Scientific, UK). Morphological features were studied using Scanning Electron Microscope (Model S4700, Hitachi, Japan) and Transmission Electron Microscope (JEOL JEM 2100) Brunauer-Emmett-Teller (BET) Specific Surface area and the nature of the porous network are studied using Nitrogen adsorption/desorption analysis recorded at 77 K using ASAP 2420 from Micromeritics.

### 2.4. Electrical conductivity analysis

The electrical conductivity of the prepared Oxygen-rich functionalized porous carbon (PJF) was examined using a homemade SS-Swagelok set-up and multimeter. For the conductivity studies, 100 mg of PJF samples (600, 700, and 800 °C) are compressed between the plungers of the Swagelok cell with the help of nuts to avoid air gaps. The nobs in the plungers are used as a current collector connected with a multimeter. The conductivity offered by each material is calculated using the equation, $\sigma = L/RA$. Where L is the thickness of the material, R is the measured resistance using multimeter and A is the area of the plungers

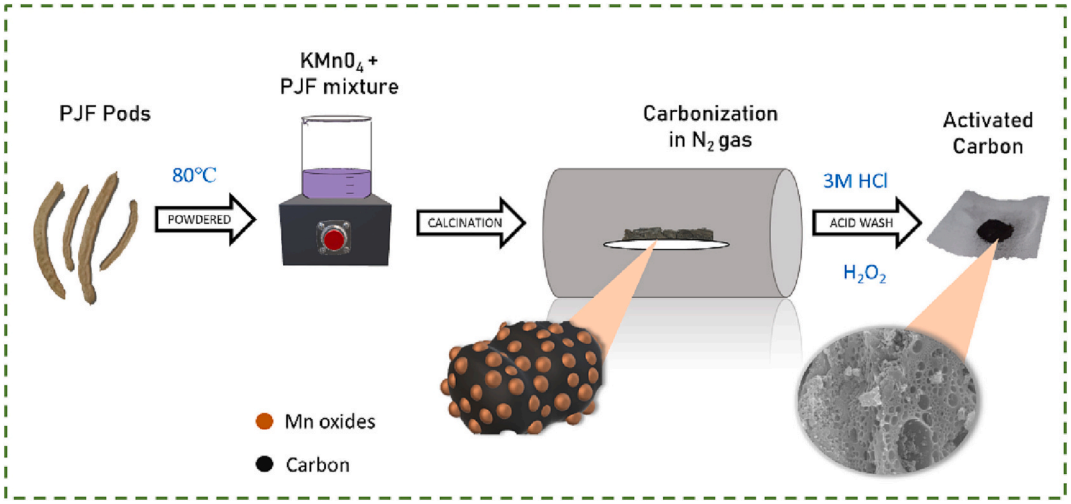


**Fig. 1.** Synthesis protocol for the oxygen-rich functionalized hierarchical porous carbon.

(diameter is 0.9 cm).

### 2.5. Electrochemical characterizations

Electrochemical impedance spectra (EIS), cyclic voltammetry (CV), and Galvanostatic charge-discharge (GCD) were conducted, and their performance was observed using the electrochemical workstation (Bio-Logic SP 150). The fundamental electrochemical characterization was performed using the three-electrode system with PJF-coated SS sheet as an active electrode, Pt wire as a counter, and saturated calomel electrode (SCE) as reference electrodes in 1 M $Na_2SO_4$ electrolyte. The specific capacitance was calculated using the Eq. (1).

$$C = \frac{I \times \Delta t}{m \times \Delta V} \tag{1}$$

Where **I** (in terms of A) is the discharge current, **Δt** (in terms of s) is the discharge time, **m** (in terms of g) is the mass of an electrode, **ΔV** is the voltage window excluding IR drop. The Energy density **E** (in terms of Wh $kg^{-1}$) and power density **P** (in terms of W $kg^{-1}$) of the symmetric supercapacitors were calculated from the following eqs. (2) and (3) respectively.

$$E = \frac{C_s \times \Delta V^2}{2 \times 3.6} \tag{2}$$

$$P = \frac{E \times 3600}{\Delta t} \tag{3}$$

## 3. Results and discussion

### 3.1. Structural and Morphological properies of PJF-X

The structural characterization of synthesized carbon was determined by XRD analysis (Fig. 2 (a)). All the XRD Patterns showed two broad peaks centered at ~29° corresponding to the (002) plane, representing the turbo static structure of carbon [46–49], and the peak at 42° corresponds to the (100) plane, which infers the presence of $sp^2$ hybridized carbon with amorphous nature. Notably, the additional peak at 16° attributed to the oxygen-rich functional groups present in the surface of carbon similar to graphene oxides [50]. Further, the (002) plane of PJF-700 is slightly shifted to 30° due to the presence of an intense OFG peak at 16° representing the uniqueness of $KMnO_4$ activation with graphitic layers [48,51].

It is well known that $KMnO_4$ provides two distinct activators of $K_2CO_3$ and $MnO_2$ during carbonization reactions. Initially, the $KMnO_4$ is

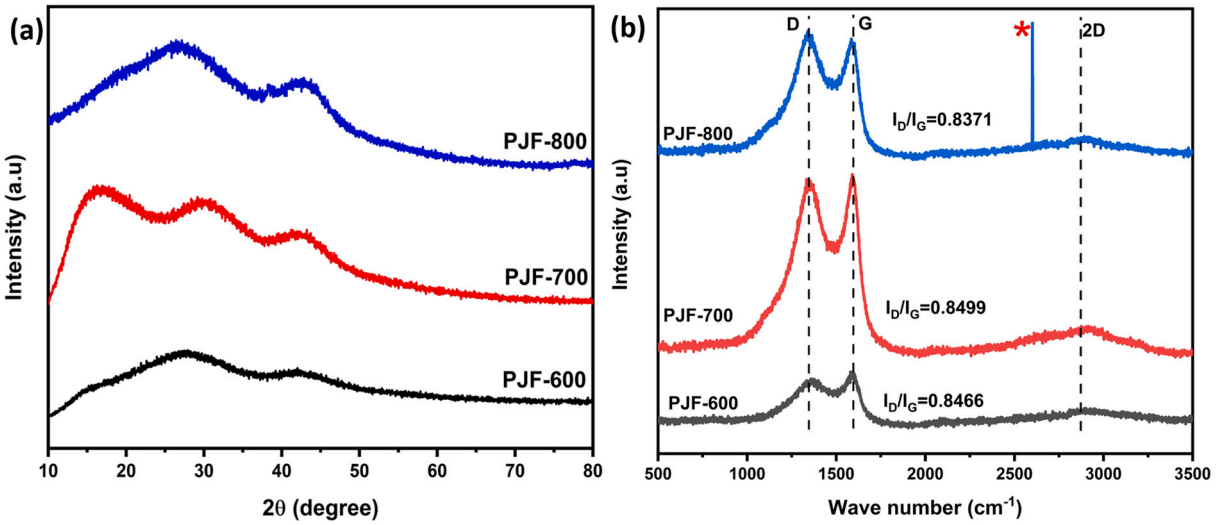


**Fig. 2.** (a) XRD pattern and (b) Raman spectra of synthesized porous carbon.

decomposed into $K_2MnO_4$ and $MnO_2$ (Eq. (4)). Subsequently, $K_2MnO_4$ decomposed into $K_2CO_3$ activator (Eq. (5)) under a carbon atmosphere.

$$2KMnO_4 \rightarrow K_2MnO_4 + MnO_2 + O_2 \quad (4)$$

$$K_2MnO_4 + C \rightarrow K_2CO_3 + MnO \quad (5)$$

Further, MnO and $CO_2$ gases were produced by reacting the activator, $MnO_2$, with carbon. Therefore, significant porosity is developed in the carbon layers while releasing the $CO_2$ gas and removing the MnO sites during washing [37]. On the other hand, the $K_2CO_3$ makes the carbon and carbon monoxide (CO) through decomposition reaction. Similarly, the $K_2CO_3$ further undergoes the decomposition reaction and ultimately producing potassium salts upto 700 °C [37]. At higher temperatures (800 °C), $K_2CO_3$ decomposes to $CO_2$ and $K_2O$, where the oxygen functionalization is reached ultimately, forming a very high intense peak at 16°. At a low activation temperature of 600 °C, the OFG was not attained due to an incomplete reaction of $K_2CO_3$ [52,53]. Further, the interplanar spacing, d was calculated from the (002) plane of PJF-600, PJF-700, and PJF-800 and found to be 0.32 nm, 0.29 nm, and 0.32 nm, respectively [54]. Although these values are around 3.0 nm, the low value of $d_{(002)}$ at 700 °C shows a higher degree of graphitization which is further obtained by calculating the amorphous degree ($F_a$) using equation no (6).

$$F_a = A_{(002)} / \left(A_{(002)} + A_{(100)}\right) \quad (6)$$

The calculated values of $F_a$ were found to be 0.85, 0.64, and 0.78, corresponding to PJF-600, PJF-700, and PJF-800, respectively [55]. The comparatively less amorphous degree of PJF-700 ensures that the sample possesses comparatively high graphitization, which is further to be confirmed by Raman spectra [55].

The structural characteristics of carbon are analyzed using the non-invasive Raman Spectroscopy and shown in Fig. 2 (b). It can be seen that the peak observed at ~1350 $cm^{-1}$, ~1600 $cm^{-1}$, and 2800 $cm^{-1}$ corresponds to the D band, G band, and the unresolved 2D band. The D band is due to the disordered carbon, whose prominence assures the amorphous nature with irregularities and the planar vibration of the $A_{1g}$ modes. The G band, known to be the intense peak, shows an $sp^2$ hybridized C atom with graphitic nature ascribed to in-plane vibration of $E_{2g}$ modes [56]. In general, the intensity ratio of the D and G band ($I_D/I_G$) is calculated to explore the degree of order of carbon structure. If the $I_D/I_G$ ratio is 1.0, it typically attributes to the amorphous nature of carbon, and the value around 0.8–0.9 features an improved graphitization degree. From Fig. 1 (b), the $I_D/I_G$ ratio of PJF-600, PJF-700, and PJF-800 is 0.846, 0.849, and 0.837, respectively. The lower $I_D/I_G$ value of ~0.84 on average show that the samples possess a high degree of graphitization, enabling high conductivity [57]. The 2D band is known to be the overtone of defect over the D band fulfilled by two phonon lattice vibrations. At high temperatures, the lowest value of $I_D/I_G$ manifests that the sample has undergone a higher degree of graphitization with a comparatively less amorphous nature. Thereby the additional peak was found in PJF-800 over ~2607 $cm^{-1}$, corresponding to a graphene-like structure (Tables 1 and 2).

The BET analysis with Nitrogen adsorption and desorption is used to reveal the porosity parameter of the carbon. Fig. 3 (a) shows a Type IV isotherm (IUPAC classification) with the hysteresis loop between the adsorption and desorption branches. In the low-pressure region ($P/P_0 < 0.01$), strong adsorption was observed with a broad knee following the hysteresis curve over the mid-range ($0.2 < P/P_0 < 0.4$) and an elevated curve over the high-pressure region ($P/P_0 = 0.9$–1.0). This behavioral pattern infers the hierarchical porous network with micropores, mesopores, and macropores in all the synthesized carbon samples [58]. The high absorption at the low-pressure region over the increase in temperature signifies the presence of micropores, notably high in PJF-800. A wide hysteresis loop from $P/P_0$0.4 to 0.99 shows the presence of mesoporous distribution, and the increase in pore volume can also be seen from $P/P_0$ >0.99 with an increase in temperature.

**Table 1**
Structural parameter from XRD and Raman analysis.

| Carbon sample | PJF-600 | PJF -700 | PJF-800 |
|---|---|---|---|
| Interplanar spacing $d_{002}$ (nm) | 0.32 | 0.29 | 0.32 |
| Amorphous degree ($F_a$) | 0.85 | 0.64 | 0.78 |
| $I_D/I_G$ ratio | 0.846 | 0.849 | 0.837 |

**Table 2**
BET Specific surface area and XPS parameters.

| Specification | PJF-600 | PJF-700 | PJF-800 |
|---|---|---|---|
| Specific surface area ($m^2g^{-1}$) | 753 | 1210 | 1910 |
| Carbon (%) | 64.8 | 59.8 | 65.9 |
| Oxygen (%) | 32.0 | 36.3 | 30.9 |
| Nitrogen (%) | 3.2 | 3.9 | 3.2 |
| O/C ratio | 0.49 | 0.60 | 0.47 |

The pore size distribution of the carbon samples was studied using the DFT method (Fig. 3(b)). The maximum peak at 2 nm corresponds to the micropores, favoring EDLC behavior. The peak around 25 nm corresponds to the mesoporous structure acting as a pool for charge storage. The extended pore distribution over 50 nm to 100 nm shows macropores acting as ion buffering reservoirs, which reduces the ionic diffusion distance and low resistance pathway. The obtained BET-specific surface area of PJF-600, PJF-700 and PJF-800 is 753.28 $m^2g^{-1}$, 1210.4 $m^2g^{-1}$ and 1910.5 $m^2g^{-1}$, respectively. Normally, the specific capacitance relies on the specific surface area of the carbon since it determines the capability of adsorbing the ions from the electrolyte. But it is important to note that the specific capacitance is not linearly dependent on the BET surface area. In addition to the high specific surface area, the porous nature of the sample must be there to predict the ionic adsorption efficiency [59]. Higher microporous volume increases BET surface, but these micropores cannot access all the ions owing to their size limit of adsorption to the largest pores. Comparatively, the higher surface area of PJF-700 (1210.4 $m^2g^{-1}$) and PJF-800 (1910.5 $m^2g^{-1}$) may result in better electrochemical activity as their pore distribution corresponds to hierarchical nature. Importantly, the obtained specific surface area is much higher than the biomass carbon derived from *Prosopis juliflora* by orthophosphoric acid ($H_3PO_4$) activation (946.06 $m^2$ $g^{-1}$) [60], zinc chloride ($ZnCl_2$) activation (1028 $m^2$ $g^{-1}$) [61], 1464.4 $m^2$ $g^{-1}$ by hard-templating method combined with a soft-templating approach (1464.4 $m^2$ $g^{-1}$) [62], KOH activation (967 $m^2$ $g^{-1}$) [63] and $KMnO_4$ activation on corn stalk reported a high specific capacitance of 1039 $m^2g^{-1}$ [40]. Therefore, from the comparative analysis of BET surface area as given in Table 2, $KMnO_4$ effectively increases the specific surface area through their uniue approach of inducing hierarchical porosity.

The morphological analysis of the synthesized carbon sample is studied through FESEM and TEM analysis. The inadequate and incomplete dispersion of PJF-600's pores is depicted in Fig. 4(a), which is the result of insufficient activation temperature. While the other images (Fig. 4b and Fig. 4c) demonstrated the greatest amount of pores. The mechanism of pore distribution has followed the conventional activation reaction process of $KMnO_4$, where the dual activators $K_2CO_3$ and $MnO_2$ react with carbon to produce oxygen-rich carbon compounds, K salts, and MnO compounds. As their morphology represents the wide distribution of pores in PJF-700 and PJF-800, their activation was complete. The residue of K salts and MnO sites are thoroughly washed out, resulting in a hierarchical porous structure. In addition, the TEM image of PJF-700 is also illustrated in Fig. 3 (d), where an uneven and wide distribution of pores were noticed.

The activated carbon samples are further subjected to elemental analysis using XPS, and the corresponding survey and deconvoluted spectra are shown in Fig. 5. Two prominent peaks are observed at the binding energies of 531 eV and 285 eV, corresponding to Oxygen (O1s) and Carbon (C1s) in the survey spectra (Fig. 5a). In addition, a small

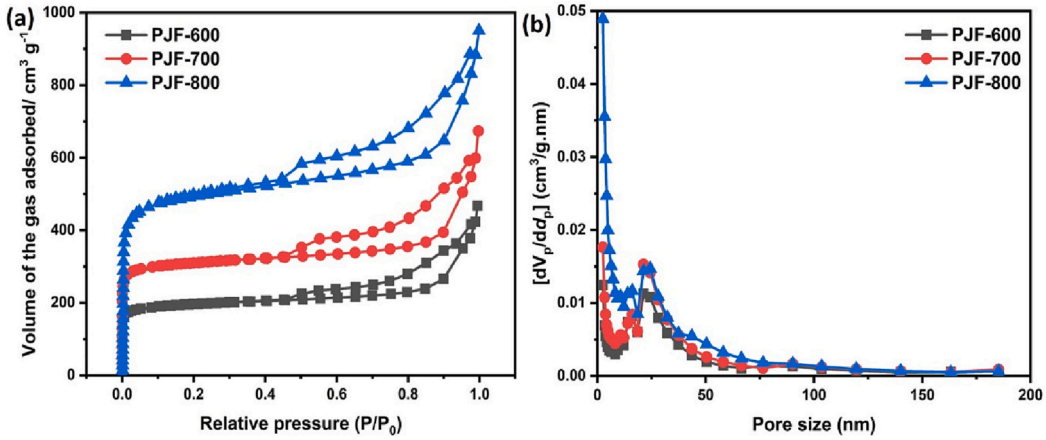


**Fig. 3.** (a) $N_2$ adsorption/ desorption isotherm and (b) pore size distribution of synthesized porous carbon.

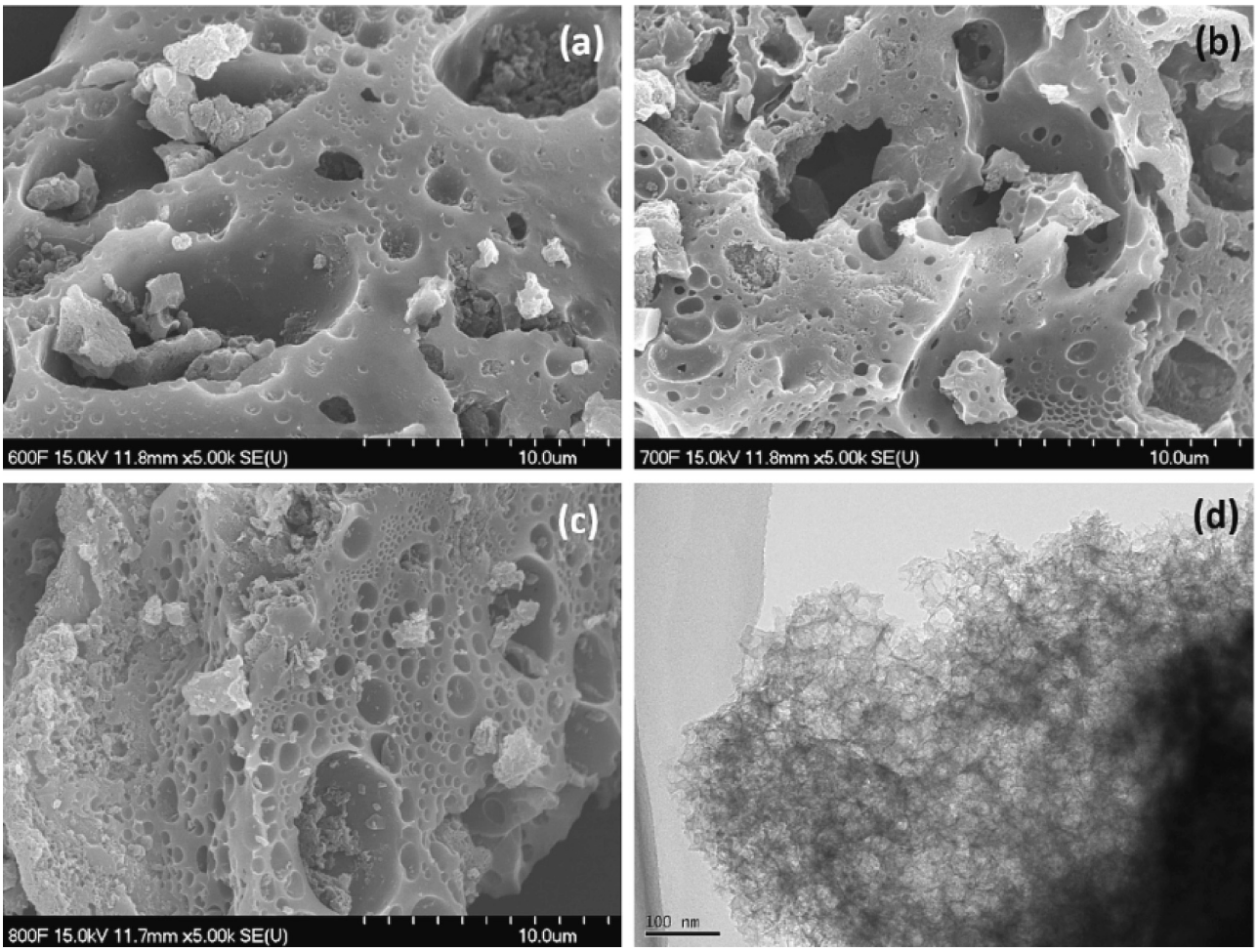


**Fig. 4.** (a-c) FESEM images of PJF-600, 700 & 800 (d) TEM image of PJF-700 sample.

peak at the binding energy of 398 eV reveals the presence of Nitrogen (N1s) in PJF-800. Importantly,the survey spectrum clearly suggests that no impurities such as Mn oxides and K salts are left after acid wash and neutralization of porous carbon samples. From the deconvoluted plot of C1s (Fig. 5b), the most prominent peak around 384.5 eV corresponds to C—C of $sp^3$ hybridized carbon, and peak around 286 and 289 eV corresponds to C—O and C═O, respectively [64]. The deconvoluted spectra of O1s (Fig. 5c) show the peaks at 530, 532, and 533 eV attributed to C═O, C—O, and —O— respectively in the O1s spectrum [65]. Similarly, two peaks in the N1s (Fig. 5d) curve correspond to Pyridinic-N at 397 eV and Graphitic —N at 401 eV [66].

The distribution percentage of Carbon, Oxygen, and Nitrogen is in Table 2, which depicts the uniqueness of PJF-700 over 60 % of carbon, 36 % of oxygen and 4 % of nitrogen. It is well known that the presence of Oxygen and Nitrogen functional groups enhances the electrochemical performance. Interestingly, PJF-700 has higher oxygen percentage than PJF-600 (~32 %) and PJF-800 (~30 %). In addition, the O/C ratio and N/C ratio were also calculated from their percentage distribution which

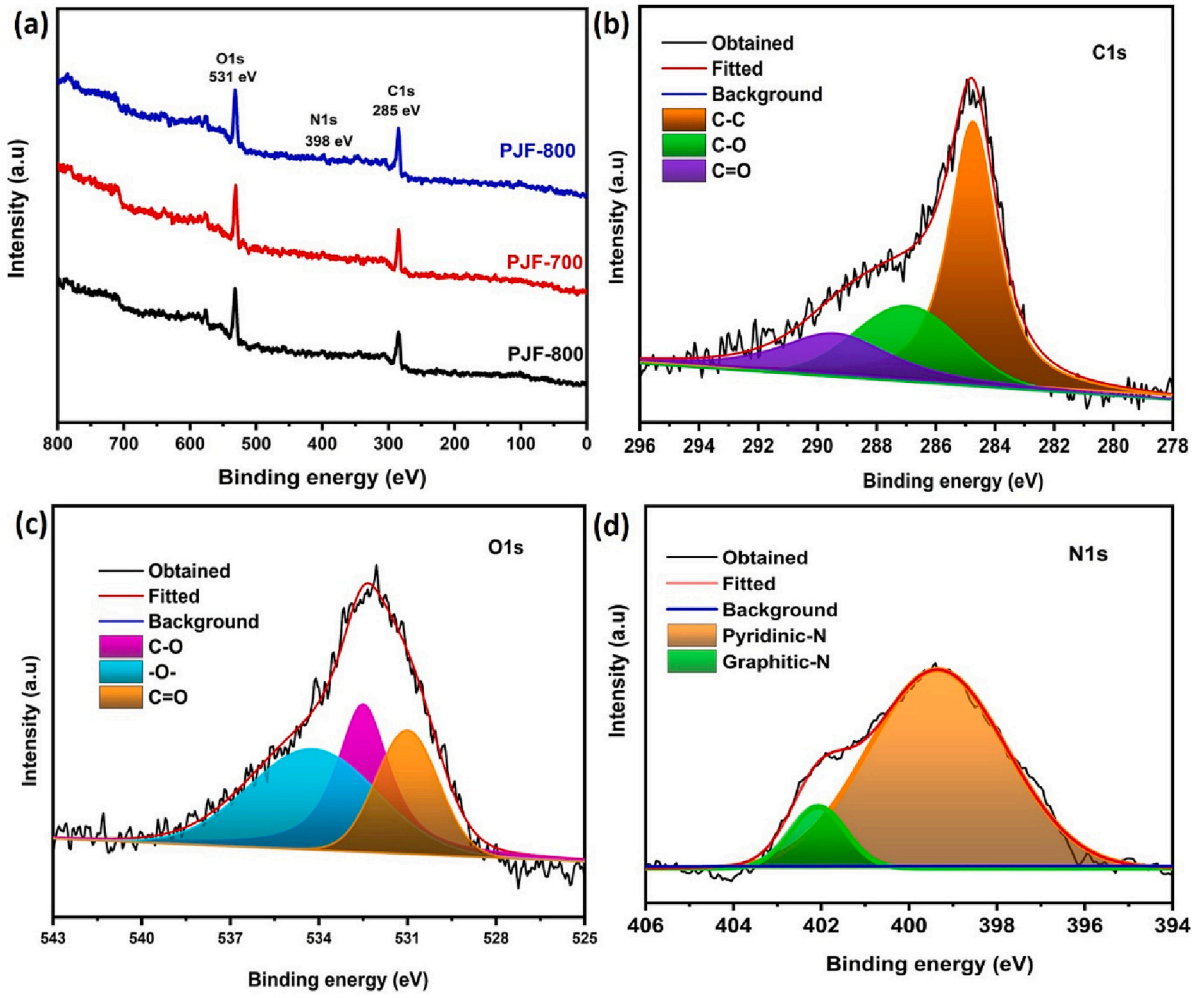


**Fig. 5.** XPS spectra of synthesized porous carbon. (a) Survey spectra of PJF-X, the deconvoluted spectra of (b) Carbon C1s, (c) Oxygen O1s, and (d) Nitrogen N1s of PJF-700.

clearly shows the higher ratio values of PJF-700 i.e., 0.6 and 0.06, respectively [67]. The obtained higher values over PJF-600 (0.49 and 0.04) and PJF-800 (0.47 and 0.04) elucidate the presence of Oxygen-rich and comparatively more nitrogen functional groups in the PJF-700 sample. Thereby increasing the wettability of electrodes and high specific capacitance through pseudo capacitance offered by surface redox reactions.

### 3.2. Electrical and electrochemical properties of PJF

The conductivity of PJF samples is measured before analyzing the electrochemical properties. The calculated electrical conductivity of PJF-600, PJF-700, and PJF-800 are $8.12 \times 10^{-4}$, $2.99 \times 10^{-2}$ and $8.13 \times 10^{-2}$ S $cm^{-1}$, respectively. It is worth noting that the electrical conductivity of the PJF materials increases with increasing carbonization temperature. Adinaveen et al. [68] reported a similar type of observation. During the high-temperature treatment, the biomass components of cellulose are decomposed into carbon which creates pores by releasing volatile gases. External pressure compresses the activated carbon to achieve a better volumetric fraction, increasing the average number of contacts to determine the apparent electrical conductivity [69,70].

The electrochemical performances of the PJF samples were analyzed using electrochemical impedance analysis, cyclic voltammetry, and galvanostatic-charge discharge profile. Electrochemical impedance spectroscopy (EIS) was initially conducted to explore the ion transport kinetics at the electrode-electrolyte interface [71]. The Nyquist plot (Fig. 6 (a)) shows a depressed semicircle at the high-frequency region and an upwards-seeming linear slope at the low-frequency region. From the Nyquist plot, solution resistance ($R_s$) at high frequency and interfacial resistance ($R_{ct}$) at mid-frequency are obtained from the X-axis intercept. The ion diffusion resistance (Ω) within the electrodes is calculated from the low-frequency slope. The equivalent circuit was built using EC lab software to obtain the above parameters. The fitted plot with its equivalent circuit is shown in the inset of the Fig. 6 (a). EIS parameters such as $R_s$ and, $R_{ct}$ values are resolved from the equivalent circuit components tabulated in Table 3. The $R_s$ value of PJF-600, PJF-700, and PJF-800 is 2.15, 0.47, and 1.91 Ω, respectively. The lower $R_s$ value of PJF-700 shows the least contribution to equivalent resistance from the electrolytes. Similarly, the charge transfer resistance ($R_{ct}$) is 15.7, 20.9, and 116.4 Ω, respectively [72]. Comparatively lower $R_{ct}$, well-defined complete semicircle, and the linear curve with the highest slope (almost vertical line) elucidates the less equivalent resistance, better double-layer capacitance, and faster ion transfer characteristics at the electrode-electrolyte interface of PJF-700 material [45]. The micropores and the mesopores enable the ions to flow and ensure maximum access to the electrodes, resulting in less resistance which means high conductivity.

Further, from the impedance results, the admittance characteristics were also obtained and are shown in Fig. 6 (b). The Knee frequency is obtained from the admittance plot, which is the maximum frequency where the resistance behavior is small, and the capacitive behavior

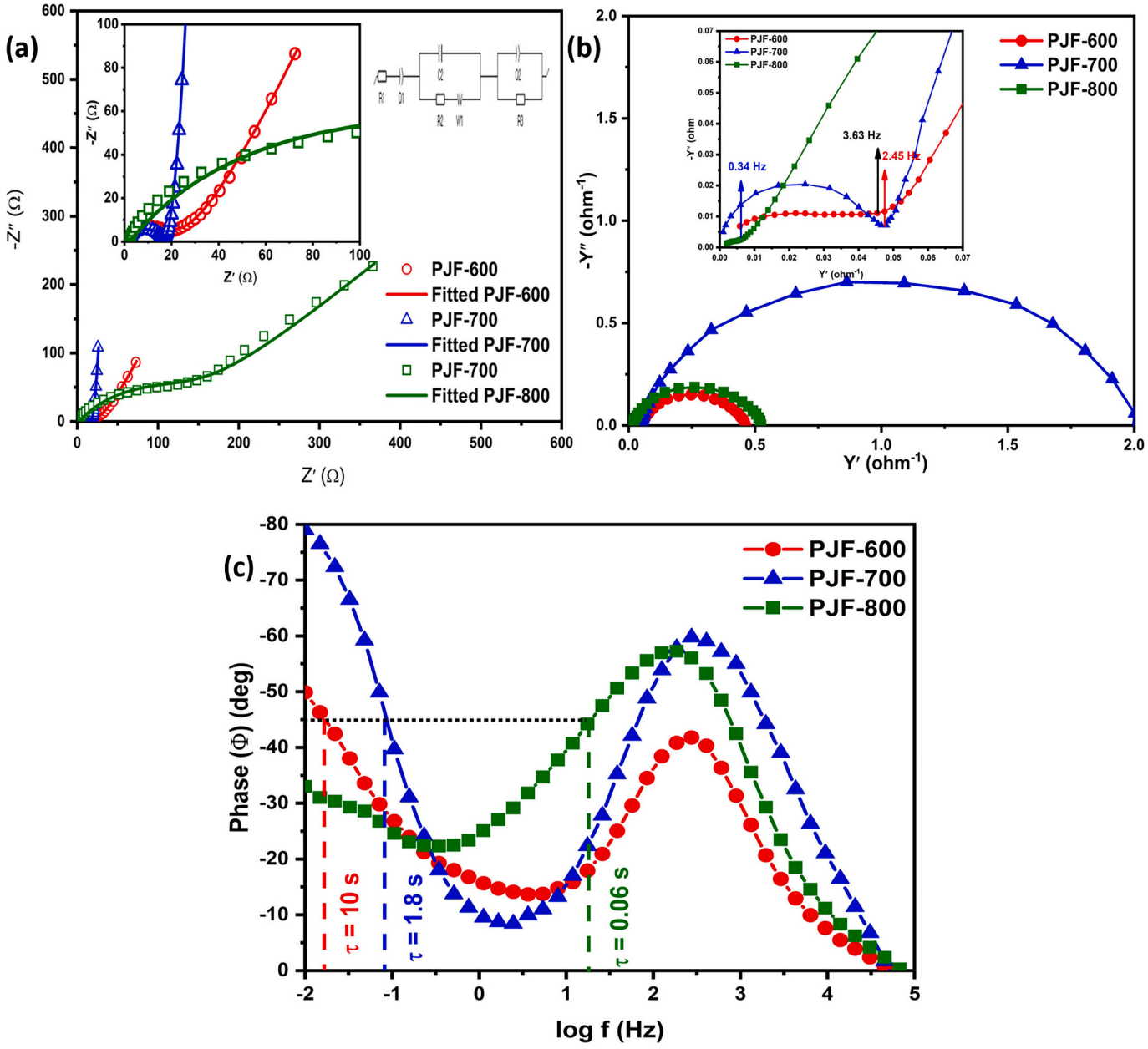


**Fig. 6.** (a) Nyquist plot, (b) Admittance plot, and (c) log f vs. phase plot of synthesized porous carbons.

**Table 3**
EIS fitted parameters.

| Sample | $R_s$ (Ω) | $R_{ct}$ (Ω) |
|---|---|---|
| PJF-600 | 2.027 | 13.72 |
| PJF-700 | 1.374 | 15.33 |
| PJF-800 | 1.667 | 130.3 |

overrides. The Knee frequencies of PJF-600, PJF-700, and PJF-800 are 3.63, 2.45, and 0.34 Hz, respectively. Despite the high Knee frequency of PJF-600, its high $R_s$ and $R_{ct}$ reduce the capacitance behavior and may result in comparatively poor electrochemical performance. From the phase angle vs. frequency plot (Fig. 6 (c)), the relaxation time (τ) was calculated at φ =45° as 0.06, 1.8, and 10 s for PJF-600, PJF-700, and PJF-800, respectively. The greater τ value ensures prolonged discharge time, which is high for PJF-800. But a typical supercapacitor is characterized by a phase angle when close to π/2 (90°) at low frequency, which can increase the capacitance [45]. Likely, the phase angle (φ) was very close to 90° for PJF-700 and <55° for the other samples, as shown in Fig. 6(c) ensuring the ideal capacitive behavior owing to the oxygen-rich functional groups and ideal hierarchical porous network. Thus, from the comprehensive analysis of electrochemical impedance results, we observe that PJF-700 exhibits the most favorable characteristics like low $R_s$ and $R_{ct}$, resulting in better conductivity, phase angle (≈90°), and improved ionic diffusion.

The current response of the prepared PJF electrodes was measured from Cyclic voltammetry (CV) at a scan rate of 5 mV/s with a potential window from 0 to 1.0 V vs. SCE [52] in 1 M-$Na_2SO_4$ electrolyte (Fig. 7 (a)). The reduction and oxidation curves of CV show a quasi-rectangular behaviour with broad humps at the initial and final voltage regions. The rectangular form over the mid-voltage region corresponds to the EDLC behavior, and the hump over the initial and final voltage regions shows the presence of OFG [44]. More convincingly, PJF-700 covers the maximum area with a high current and provided high specific capacitance of 94 F/g, roughly twice the specific capacitance offered by PJF-600 (54 F/g) and PJF-800 (59 F/g). The CV profile of PJF-700 was

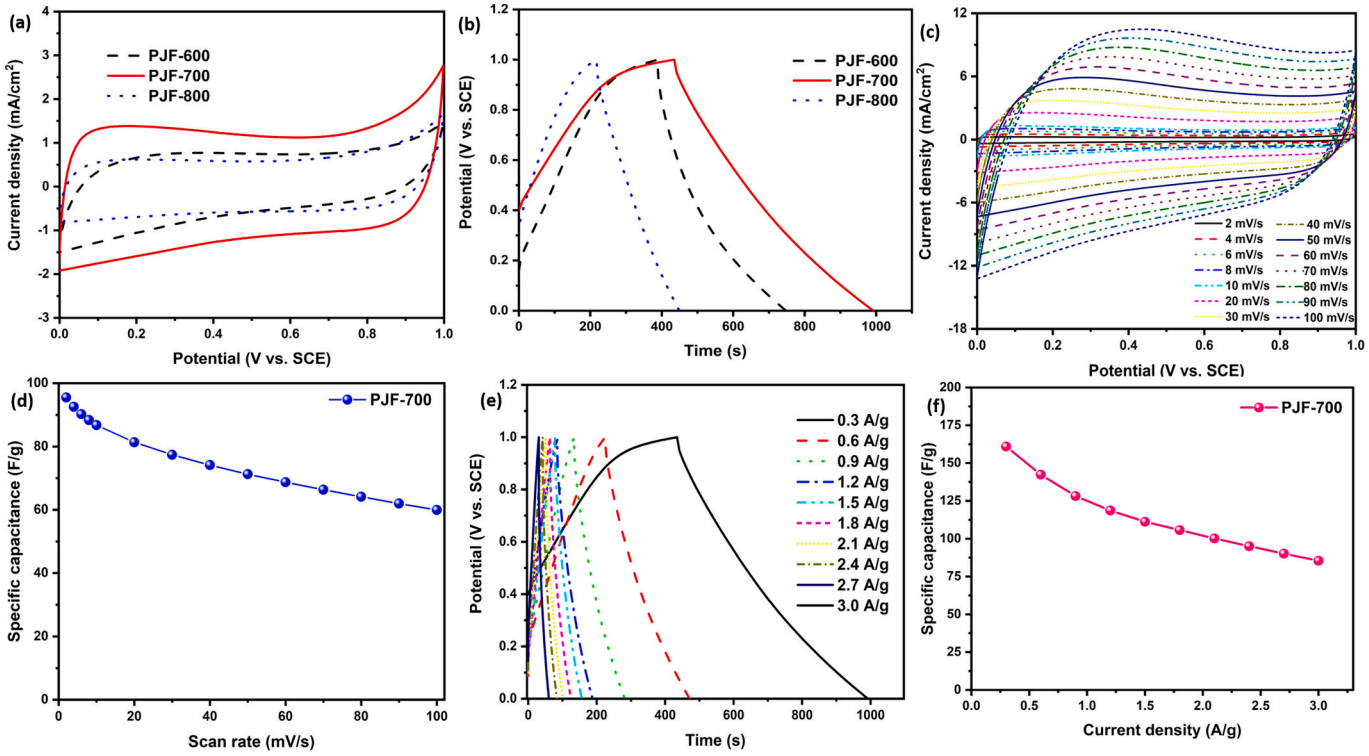


**Fig. 7.** a) Cyclic voltammograms of PJF electrodes measured at 5 mV/s, (b) GCD curves of PJF electrodes measured at 0.3 A/g, the representative (c) CV curves at different scan rates and (e) GCD curve at different current densities and the corresponding (d, f) specific capacitance values of PJF-700 electrode.

well maintained even at a high scan rate of 100 mV/s, as shown in Fig. 7 (c) with a uniform deterioration of specific capacitance from 95.5 F/g @ 2 mV/s to 60 F/g @100 mV/s with over 62.8 % of retention observed from Fig. 7(d). Hence it is evident from the CV study that PJF-700 offers better double-layered capacitance owing to its stable and uniform porosity with improved surface area.

The galvanostatic charge-discharge (GCD) performance was also studied further to facilitate the charge storage capacitance of PJF electrodes. Fig. 7(b) shows the GCD performance at a current density of 0.3 A/g. GCD curve was witnessed to be partially triangular with a slight forward hump over the apex of the triangle, which again confirms the contribution of both the EDLC and pseudocapacitive behavior. The calculated specific capacitance of PJF-600, PJF-700, and PJF-800 are 104, 161, and 70 F/g. It is pretty evident from the above values that the better Impedance characteristics, combination of pseudo and electric double layer capacitance, and Oxygen-rich functional groups had attributed to the enhanced specific capacitance of PJF-700 around 45 % over the other electrodes of PJF-600 and PJF-800. To further validate the obtained GCD results, the study is repeated with different current densities from 0.3 A/g to 3.0 A/g for PJF-700 (Fig. 7(e)), and their specific capacitance response shown in Fig. 7(f). The initial specific capacitance of 161 F/g at 0.3 A/g decreased to 85 F/g at 3 A/g. Around 50 % of the specific capacitance was retained while increasing the current density to 10 times its initial value. For high specific capacitance, the diffusion of ions from the electrolyte to the material through the pores has to be slowly mediated and highly significant in low current density [14]. At high current density, the diffusion process is very rapid, where the ionic motion is fast through the pores and not able to access the complete material, thereby reducing the specific capacitance [72]. Therefore, the improved electrochemical performance of PJF-700 in the three-electrode system with the specific capacitance of 161 F/g at the current density of 0.3 A/g is attributed to the oxygen-rich functional groups, optimized specific surface area, ideal hierarchical porous network, and best EIS analysis.

### 3.3. Electrochemical analysis of PJF-based symmetric supercapacitor

For real-time applications, the symmetric supercapacitor was constructed using the combinations of PJF-700 (PJF-700||PJF-700), The CV and GCD analysis were conducted to reveal the specific capacitance of the symmetric cell PJF-700||PJF-700 in 1 M $Na_2SO_4$ electrolyte. In Fig. 8 (a), CV curve was analyzed in different scan rates ranging from 10 mV/s to 100 mV/s, inferring that the typical EDLC behavior (rectangular) of full cell withstand up to the operating potential of 1.8 V [52]. Corresponding Specific capacitance vs. Scan rate is plotted to show a high specific capacitance of 58 F/ g at the scan rate of 10 mV/s which was reduced to 42 F/g at the scan rate of 100 mV/s (Fig. 8(b)). Even at a very high scan rate (100 mV/s), the material could hold 73 % of the initial specific capacitance. Similarly, the GCD profile of PJF-700||PJF-700 is measured for different current densities from 0.5 A/g to 5 A/g (Fig. 8 (c)). At an initial current density of 0.5 A/g the constructed symmetric cell exhibited a maximum capacitance of 58.5 F/g. A standard decrement of specific capacitance to 38 F/g was observed even at 5 A/g, as shown in Fig. 7 (d). Owing to the high operating voltage, the PJF-700|| PJF-700 cell achieved a significant energy density of 13.13 Wh $kg^{-1}$ (with a power density of 450 W $kg^{-1}$) at a current rate of 0.5 A/g. Finally, the Ragone plot Fig. 8(e) between Energy density vs. power density clearly represents the retention of energy density over high power density, the maximum energy density of 13.13 Wh $kg^{-1}$ at a power density of 450 W $kg^{-1}$ with remarkable stability of ~75 % over 5000 cycles Fig. 8 (f).

To support the strength of the working electrode, the EIS studies were conducted after 5000 cycles and compared with the plot before cycles, which shows almost equal $R_s$ but comparatively less $R_{ct}$, which may be attributed to the accumulation of ions on the porous carbon surface due to repeated charge-discharge cycles and thereby reducing its charge transfer resistance. (inset: Fig. 8. (f)) [53]. In order to compare the sifnificant energy density of our work the performance of previously reported works are tabulated (Table 4).

The significant electrochemical properties of PJF-700 electrode are

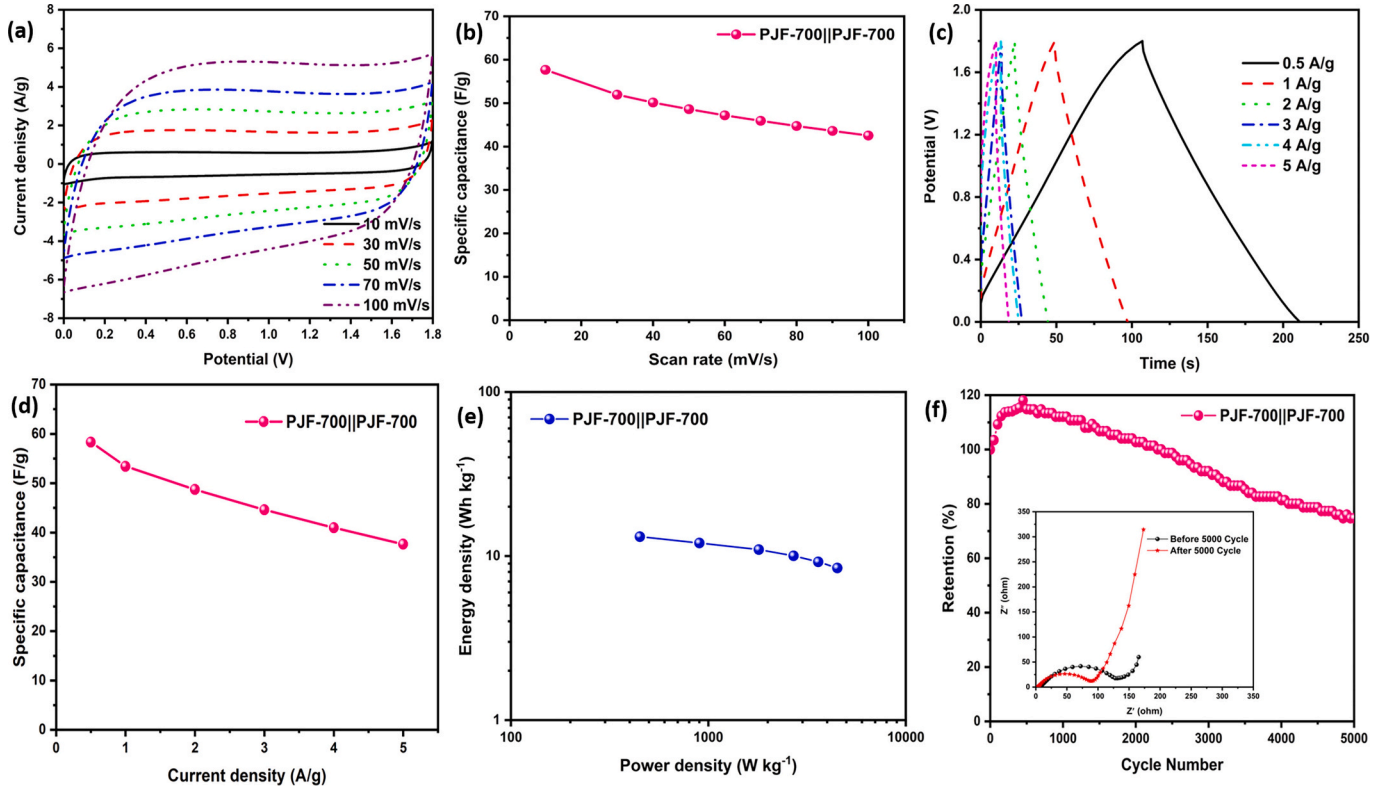


**Fig. 8.** *Electrochemical analysis of full cell. (PJF-700||PJF-700)* a) CV curve at different scan rates and the corresponding (b) specific capacitance values, (c) GCD curves of symmetric device at different current densities and the corresponding (d) specific capacitance values, (e) Ragone plot and (f) capacity retention behaviour for 5000 cycles (inset: EIS curve of the fabricated symmetric cell before and after cycling).

**Table 4**
Comparison of electrochemical parameters with other biomass derived carbon and its conditions.

| Precursor | Activating Agent | Electrolyte | Current density (A $g^{-1}$) | Energy density (Wh $kg^{-1}$) | Power density (W $kg^{-1}$) | Reference |
|---|---|---|---|---|---|---|
| Bamboo | HF/HCl | 3 M KOH | 0.5 | 10.9 | 63 | [73] |
| Cigarette filters | KOH | 6 M KOH | 0.25 | 7.2 | 127 | [74] |
| Charcoal | – | 2 mM-HQ/2 mM-PPD/1 M-$H_2SO_4$ | 2 | 1.85 | 150 | [75] |
| Hazelnut | KOH | 1 M $H_2SO_4$ | 1 | 3.47 | 100 | [76] |
| Palm oil | HF/$CaCl_2$ | 6 M KOH | 0.5 | 5.11 | 230 | [77] |
| Palm fruit | KOH/$CO_2$ | 1 M $H_2SO_4$ | – | 4.297 | 173 | [78] |
| *Prosopis juliflora* (Pod) | KOH | 1 M $H_2SO_4$ | 1.3 | 10.8 | 694 | [63] |
| *Prosopis juliflora* (stem) | KOH | 1 M $H_2SO_4$ | 0.5 | 7.81 | 150 | [79] |
| Coal | KOH | 6 M KOH | 0.2 | 4.2 | 100 | [80] |
| Lignite | KOH/$H_2O$ | 6 M KOH | 0.5 | 9.8 | 250 | [81] |
| *Prosopis juliflora* | $KMnO_4$ | 1 M $Na_2SO_4$ | 0.5 | 13.13 | 450 | |
| | | | 2 | 10.96 | 1800 | This work |

achieved through appreciable individual characteristics such as (i) ideal hierarchical porous network with micropores, mesopores, and macropores in PJF-700 (ii) large BET specific surface area of 1210.4 $m^2g^{-1}$ (iii) ~36 % of functional groups present in the synthesized carbon consist of oxygen-rich functional groups which can support pseudo-capacitance, above all they provide an acceptable specific capacitance and reasonable stability over a large number of cycles. Moreover, the collective ionic and electrical conductivity of $KMnO_4$ assisted Oxygen-rich functionalized porous carbon (PJF-700) supports better EDLC behavior. As a combination in full cell symmetric supercapacitor (PJF-700 ||PJF-700) results in a significant energy density of 13.13 Wh $kg^{-1}$ at a power density of 450 W $kg^{-1}$. This was achieved through less solution and charge transfer resistance which supports increasing the conductivity of the sample. In addition, the combination also offers high ion transport characteristics at the electrode-electrolyte interface, which is evident through EIS studies that offer excellent electrochemical performance.

## 4. Conclusion

In summary, it is clearly demonstrated that the synthesized oxygen-rich hierarchical porous network through one-step activation using $KMnO_4$ resulted in a better energy density of 13.13 Wh $kg^{-1}$ at a power density of 450 W $kg^{-1}$ and 70 % specific capacitance retention after 5000 cycles in PJF-700 || PJF-700 symmetric cell. Notably, the synthesized sample reports a hierarchical porous network which was evident from BET analysis with a high specific surface area of 1210.4 $m^2g^{-1}$ and high oxygen functional groups (36 %) in PJF-700. Impedance analysis also supports the better performance of PJF-700 with less solution and charge transfer resistance. Therefore, the better electrochemical values of PJF-700 are obvious from the Oxygen-rich functional groups and ideal hierarchical porous network. Through this work, we have encountered a useful by-product of the invasive weed, PJF with promising energy storage applications.

## CRediT authorship contribution statement

**K. Vignesh:** Investigation, Formal analysis, Writing – original draft, Visualization. **M. Ganeshbabu:** Investigation, Formal analysis, Writing – original draft, Visualization. **N. Prasanna Naga Puneeth:** Investigation, Formal analysis, Visualization. **T. Mathivanan:** Investigation, Formal analysis, Visualization. **B. Ramkumar:** Resources. **Yun Sung Lee:** Resources. **R. Kalai Selvan:** Conceptualization, Investigation, Formal analysis, Writing – review & editing, Supervision, Funding acquisition.

## Declaration of competing interest

The authors declare that they have no known competing financial interests or personal relationships that could have appeared to influence the work reported in this paper.

## Data availability

Data will be made available on request.

## Acknowledgment

Mr. K. Vignesh and Dr. R. Kalai Selvan would like to thank Tamil Nadu State Council for Science and Technology (TNSCST), Tamil Nadu, for providing funds (PS-477) under Student Project Scheme. Prof. Yun-Sung Lee acknowledges the financial support from the National Research Foundation of Korea (NRF) grant funded by the Korean government (Ministry of Science, ICT & Future Planning) (No. RS-2023-00208361).

## References

[1] G.Z. Wei Zhou, H. Jin, S. Jiang, H.C. Huang, Chunmei Zhang Minjie, Bio-template synthesis of $V_2O_3$@carbonized Dictyophora composites for advanced aqueous zinc-ion batteries Wei, Molecules 28 (2023) 2147, https://doi.org/10.3390/molecules28052147.

[2] X. Wen, J. Luo, K. Xiang, W. Zhou, C. Zhang, H. Chen, High-performance monoclinic $WO_3$ nanospheres with the novel $NH^{4+}$ diffusion behaviors for aqueous ammonium-ion batteries, Chem. Eng. J. 458 (2023), 141381, https://doi.org/10.1016/j.cej.2023.141381.

[3] D. Li, H. Guo, S. Jiang, G. Zeng, W. Zhou, Z. Li, Microstructures and electrochemical performances of $TiO_2$-coated mg-Zr co-doped NCM as a cathode material for lithium-ion batteries with high power and long circular life, New J. Chem. 45 (2021) 19446–19455, https://doi.org/10.1039/d1nj03740d.

[4] S. Satpathy, N.K. Misra, D. kumar Shukla, V. Goyal, B.K. Bhattacharyya, C. S. Yadav, An in-depth study of the electrical characterization of supercapacitors for recent trends in energy storage system, J. Energy Storage 57 (2023), 106198, https://doi.org/10.1016/j.est.2022.106198.

[5] S.A. Bhat, V. Kumar, S. Kumar, A.E. Atabani, I. Anjum Badruddin, K.J. Chae, Supercapacitors production from waste: a new window for sustainable energy and waste management, Fuel. 337 (2023), 127125, https://doi.org/10.1016/j.fuel.2022.127125.

[6] Y. Yang, D. Chen, W. Han, Y. Cheng, B. Sun, C. Hou, G. Zhao, D. Liu, G. Chen, J. Han, X. Zhang, Nature-inspired self-activation method for the controllable synthesis of highly porous carbons for high-performance supercapacitors, Carbon N. Y. 205 (2023) 1–9, https://doi.org/10.1016/j.carbon.2023.01.013.

[7] L. Yao, J. Jiang, H. Peng, H. Yang, S. Liu, X. Wen, P. Cai, Y. Zou, H. Zhang, F. Xu, L. Sun, X. Lu, Glutinous rice-derived carbon material for high-performance zinc-ion hybrid supercapacitors, J. Energy Storage 58 (2023), 106378, https://doi.org/10.1016/j.est.2022.106378.

[8] H. Wang, H. Wang, F. Ruan, Q. Feng, Y. Wei, J. Fang, High-porosity carbon nanofibers prepared from polyacrylonitrile blended with amylose starch for application in supercapacitors, Mater. Chem. Phys. 293 (2023), 126896, https://doi.org/10.1016/j.matchemphys.2022.126896.

[9] S. Jiao, Y. Yao, J. Zhang, L. Zhang, C. Li, H. Zhang, X. Zhao, H. Chen, J. Jiang, Nano-flower-like porous carbon derived from soybean straw for efficient N-S co-doped supercapacitors by coupling in-situ heteroatom doping with green activation method, Appl. Surf. Sci. 615 (2023), 156365, https://doi.org/10.1016/j.apsusc.2023.156365.

[10] H. Wang, H. Wang, R. Sun, L. Yao, H. Zuo, F. Ruan, Q. Feng, J. Wang, Preparation of hierarchical micro-meso porous carbon and carbon nanofiber from polyacrylonitrile/polysulfone polymer via one-step carbonization for supercapacitor electrodes, Electrochim. Acta 441 (2022), 141827, https://doi.org/10.2139/ssrn.4260561.

[11] K. Gajewska, A. Moyseowicz, D. Minta, Effect of electrolyte and carbon material on the electrochemical performance of high-voltage aqueous symmetric supercapacitors, J. Mater. Sci. 58 (2023) 1721–1738, https://doi.org/10.1007/s10853-023-08148-5.

[12] T. Gajalakshmi, T. Kalaivani, N. Thuy Lan Chi, K. Brindhadevi, Investigation on carbon derived from casuarina bark using microwave activation for high performance supercapacitors, Fuel 337 (2023), 127078, https://doi.org/10.1016/j.fuel.2022.127078.

[13] H. Liu, F. Zhang, X. Lin, J. Wu, J. Huang, A hierarchical integrated 3D carbon electrode derived from gingko leaves via hydrothermal, Nanoscale Adv 5 (2023) 786–795, https://doi.org/10.1039/d2na00758d.

[14] L. Wang, R. Liu, Knitting controllable oxygen-functionalized carbon fiber for ultrahigh capacitance wire-shaped supercapacitors, ACS Appl. Mater. Interfaces 12 (2020) 44866–44873, https://doi.org/10.1021/acsami.0c14221.

[15] Weiwei Zhu, D. Shen, H. Xie, Combination of chemical activation and nitrogen doping toward porous carbon material from Houttuynia Cordata for supercapacitors, J. Energy Storage 60 (2022), 106595, https://doi.org/10.2139/ssrn.4246557.

[16] J. Zhao, W. Zhang, D. Shen, H. Zhang, Z. Wang, Preparation of porous carbon materials from black liquor lignin and its utilization as $CO_2$ adsorbents, J. Energy Inst. 107 (2023), 101179, https://doi.org/10.1016/j.joei.2023.101179.

[17] L. Luo, Y. Lan, Q. Zhang, J. Deng, Q. Zeng, H. Gao, G. Du, W. Zhao, Enhanced capacitance of phosphorus, nitrogen, and oxygen tri-doped balsa wood-based porous carbon for supercapacitors, J. Energy Storage 58 (2023), 106339, https://doi.org/10.1016/j.est.2022.106339.

[18] J. Peng, X. Dai, J. Huang, J. Zeng, L. Zheng, H. Chen, High-yield preparation of B/N co-doped porous carbon nanosheets from a cross-linked boronate polymer for supercapacitor applications, J. Energy Storage 59 (2023), 106498, https://doi.org/10.1016/j.est.2022.106498.

[19] F. Zeng, Z. Meng, Z. Xu, J. Xu, W. Shi, H. Wang, X. Hu, H. Tian, Biomass-derived porous activated carbon for ultra-high performance supercapacitor applications and high flux removal of pollutants from water, Ceram. Int. 49 (2023) 15377–15386, https://doi.org/10.1016/j.ceramint.2023.01.122.

[20] M. Wang, J. Yang, S. Liu, X. Che, S. He, G. Chen, J. Qiu, Nitrogen-doped porous carbon electrode for aqueous iodide redox supercapacitor, Chem. Eng. J. 451 (2023), 138501, https://doi.org/10.1016/j.cej.2022.138501.

[21] D.B. Basha, S. Ahmed, A. Ahmed, M.A. Gondal, Recent advances on nitrogen doped porous carbon micro-supercapacitors: new directions for wearable electronics, J. Energy Storage 60 (2023), 106581, https://doi.org/10.1016/j.est.2022.106581.

[22] J. Du, L. Liu, Y. Yu, Y. Zhang, A. Chen, "Dissolution-reassembly" for N-doped hollow micro/meso-carbon spheres with high supercapacitor performance, Chin. Chem. Lett. 30 (2019) 1423–1427, https://doi.org/10.1016/j.cclet.2019.03.004.

[23] S. Zhou, C. Li, G. Gao, H. Fan, X. Hu, Bio-based resins with tannin and hydroxymethylfurfural derived high-yield carbon for Zn-ion hybrid supercapacitors, J. Clean. Prod. 389 (2023), 136067, https://doi.org/10.1016/j.jclepro.2023.136067.

[24] H. Luo, Z. Liu, L. Chao, X. Wu, X. Lei, Z. Chang, X. Sun, Synthesis of hierarchical porous N-doped sandwich-type carbon composites as high-performance supercapacitor electrodes, J. Mater. Chem. A 3 (2015) 3667–3675, https://doi.org/10.1039/c4ta05843g.

[25] N.A. Rashidi, S. Yusup, Recent methodological trends in nitrogen–functionalized activated carbon production towards the gravimetric capacitance: a mini review, J. Energy Storage 32 (2020), 101757, https://doi.org/10.1016/j.est.2020.101757.

[26] Q. Wang, J. Yan, Z. Fan, Nitrogen-doped sandwich-like porous carbon nanosheets for high volumetric performance supercapacitors, Electrochim. Acta 146 (2014) 548–555, https://doi.org/10.1016/j.electacta.2014.09.036.

[27] B. Xu, S. Yue, Z. Sui, X. Zhang, S. Hou, G. Cao, Y. Yang, What is the choice for supercapacitors: graphene or graphene oxide? Energy Environ. Sci. 4 (2011) 2826–2830, https://doi.org/10.1039/c1ee01198g.

[28] J.V. Guerrera, J.N. Burrow, J.E. Eichler, M.Z. Rahman, M.V. Namireddy, K. A. Friedman, S.S. Coffman, D.C. Calabro, C.B. Mullins, C.B. Mullins, Evaluation of two potassium-based activation agents for the production of oxygen- and nitrogen-doped porous carbons, Energy Fuel 34 (2020) 6101–6112, https://doi.org/10.1021/acs.energyfuels.0c00427.

[29] R. Bhattacharya, A review on production and application of activated carbon from discarded plastics in the context of 'waste treats waste, J. Environ. Manag. 325 (2023) 116613, https://doi.org/10.1016/j.jenvman.2022.116613.

[30] A.B. Fuertes, G.A. Ferrero, N. Diez, M. Sevilla, A green route to high-surface area carbons by chemical activation of biomass-based products with sodium thiosulfate, ACS Sustain. Chem. Eng. 6 (2018) 16323–16331, https://doi.org/10.1021/acssuschemeng.8b03264.

[31] M. Thenappan, K. Mathiyalagan, M. Abdollahifar, S. Rengapillai, Structural and electrochemical properties of Musa acuminata fiber derived hard carbon as anodes of sodium-ion batteries, Energies 16 (2023) 979. doi.org/10.3390/en16020979.

[32] Y. Li, Y. Wang, N. Liu, B. Wang, R. Dong, Nitrogen and sulfur co-doped microporous carbon prepared by a couple of activating and functionalized reagents for efficient $CO_2$ capture and selective $CO_2/CH_4$ separation, Colloids Surf. A Physicochem. Eng. Asp. 658 (2023), 130732, https://doi.org/10.1016/j.colsurfa.2022.130732.

[33] C. Saka, İ. Teğin, K. Kahvecioğlu, Sulphur-doped carbon particles from almond shells as cheap adsorbent for efficient Cd(II) adsorption, Diam. Relat. Mater. 131 (2023) 109542, https://doi.org/10.1016/j.diamond.2022.109542.

[34] J.H. Kim, S.Y. Hwang, J.E. Park, G.B. Lee, H. Kim, S. Kim, B.U. Hong, Impact of the oxygen functional group of nitric acid-treated activated carbon on KOH activation reaction, Carbon Lett. 29 (2019) 281–287, https://doi.org/10.1007/s42823-019-00024-0.

[35] M. Jerigová, M. Odziomek, N. López-Salas, "We are here!" oxygen functional groups in carbons for electrochemical applications, ACS Omega 7 (2022) 11544–11554, https://doi.org/10.1021/acsomega.2c00639.
[36] B. Xue, J. Xu, R. Xiao, Ice template-assisting activation strategy to prepare biomass-derived porous carbon cages for high-performance Zn-ion hybrid supercapacitors, Chem. Eng. J. 454 (2023), 140192, https://doi.org/10.1016/j.cej.2022.140192.
[37] D. Qiu, N. Guo, A. Gao, L. Zheng, W. Xu, M. Li, F. Wang, R. Yang, Preparation of oxygen-enriched hierarchically porous carbon by $KMnO_4$ one-pot oxidation and activation: mechanism and capacitive energy storage, Electrochim. Acta 294 (2019) 398–405, https://doi.org/10.1016/j.electacta.2018.10.049.
[38] L. Zheng, W.B. Li, J.L. Chen, Nitrogen doped hierarchical activated carbons derived from polyacrylonitrile fibers for $CO_2$ adsorption and supercapacitor electrodes, RSC Adv. 8 (2018) 29767–29774, https://doi.org/10.1039/c8ra04367a.
[39] Y. Yao, Y. Yu, C. Du, L. Wan, Y. Zhang, J. Chen, T. Xiao, M. Xie, Superbases-templated carbons doped with electrochemically active oxygen as advanced supercapacitor electrodes, J. Colloid Interface Sci. 630 (2023) 487–496, https://doi.org/10.1016/j.jcis.2022.10.106.
[40] R. Zhong, H. Zhang, Y. Zhang, P. Yue, X. Wu, $KMnO_4$-assisted synthesis of hierarchical porous carbon with ultrahigh capacitance for supercapacitor, J. Energy Storage 51 (2022), 104346, https://doi.org/10.1016/j.est.2022.104346.
[41] F. Tavakoli Foroushani, H. Tavanai, F.A. Hosseini, An investigation on the effect of $KMnO_4$ on the pore characteristics of pistachio nut shell based activated carbon, Microporous Mesoporous Mater. 230 (2016) 39–48, https://doi.org/10.1016/j.micromeso.2016.04.030.
[42] X. Gan, R. Yuan, J. Zhu, Q. Li, T. Tang, F. Qin, L. Zhu, J. Zhang, L. Wang, S. Zhang, H. Song, D. Jia, Ultra-fine carbon nanosheets from coal oxidation for tri-functional improvement of carbon nanofiber fabrics, Carbon N. Y. 201 (2023) 381–389, https://doi.org/10.1016/j.carbon.2022.09.022.
[43] K.K. Li, G.Y. Liu, L.S. Zheng, J. Jia, Y.Y. Zhu, Y.T. Zhang, Coal-derived carbon nanomaterials for sustainable energy storage applications, Xinxing Tan Cailiao/New Carbon Mater. 36 (2021) 133–154, https://doi.org/10.1016/S1872-5805(21)60010-0.
[44] F.R.M.S. Raj, G. Boopathi, D. Kalpana, N.V. Jaya, A. Pandurangan, Sustainable development through restoration of Prosopis juliflora species into activated carbon as electrode material for supercapacitors, Diam. Relat. Mater. 121 (2022), 108767, https://doi.org/10.1016/j.diamond.2021.108767.
[45] S. Shanmugapriya, S. Surendran, Y.S. Lee, R.K. Selvan, Improved surface charge storage properties of Prosopis juliflora (pods) derived onion–like porous carbon through redox-mediated reactions for electric double layer capacitors, Appl. Surf. Sci. 492 (2019) 896–908, https://doi.org/10.1016/j.apsusc.2019.06.147.
[46] T. Ai, Z. Wang, H. Zhang, F. Hong, X. Yan, X. Su, Novel synthesis of nitrogen-containing bio-phenol resin and its molten salt activation of porous carbon for supercapacitor electrode, Materials (Basel) 12 (2019) 1986, https://doi.org/10.3390/ma12121986.
[47] L.H. Nguyen, T.M.P. Nguyen, H.T. Van, X.H. Vu, T.L.A. Ha, T.H.V. Nguyen, X. H. Nguyen, X.C. Nguyen, Treatment of hexavalent chromium contaminated wastewater using activated carbon derived from coconut shell loaded by silver nanoparticles: batch experiment, Water Air Soil Pollut 230 (2019) 68, https://doi.org/10.1007/s11270-019-4119-8.
[48] K. Krishnamoorthy, M. Veerapandian, K. Yun, S.J. Kim, The chemical and structural analysis of graphene oxide with different degrees of oxidation, Carbon N. Y. 53 (2013) 38–49, https://doi.org/10.1016/j.carbon.2012.10.013.
[49] D.B. Schüpfer, F. Badaczewski, J. Peilstöcker, J.M. Guerra-Castro, H. Shim, S. Firoozabadi, A. Beyer, K. Volz, V. Presser, C. Heiliger, B. Smarsly, P.J. Klar, Monitoring the thermally induced transition from $sp^3$-hybridized into $sp^2$-hybridized carbons, Carbon N. Y. 172 (2021) 214–227, https://doi.org/10.1016/j.carbon.2020.09.063.
[50] F. ullah Khan, S. Mahmood, Z. Ahmad, T. Mahmood, Z.A. Nizami, Graphene oxide synthesis by facile method and its characterization, Open J. Chem. 2 (2019) 11–15, https://doi.org/10.30538/psrp-ojc2019.0008.
[51] K. Krishnamoorthy, M. Veerapandian, L. Zhang, K. Yun, Antibacterial efficiency of graphene nanosheets against pathogenic bacteria via lipid peroxidation, J. Phys. Chem. C 116 (2012) 17280–17287. https://doi.org/10.1021/jp3047054.
[52] R. Taslim, M.N. Sari, Apriwandi Agustino, E. Taer, Electrode of supercapacitor synthesized from leaf bunch of oil palm for enhancing capacitive properties, AIP Conf. Proc. 2219 (2020) 050004, https://doi.org/10.1063/5.0003167.
[53] R. Azargohar, A.K. Dalai, Biochar as a precursor of activated carbon, in: Applied Biochemistry and Biotechnology, Twenty-Seventh Symp. Biotechnol. Fuels Chem. ABAB Symp vol. 131, 2006, pp. 762–773. https://link.springer.com/chapter/10.1007%2F978-1-59745-268-7_62.
[54] L. Sun, C. Tian, M. Li, X. Meng, L. Wang, R. Wang, J. Yin, H. Fu, From coconut shell to porous graphene-like nanosheets for high-power supercapacitors, J. Mater. Chem. A 1 (2013) 6462–6470, https://doi.org/10.1039/c3ta10897j.
[55] M. Singh, R. Vander Wal, Nanostructure quantification of carbon blacks, C J. Carbon Res. 5 (2018) 2, https://doi.org/10.3390/c5010002.
[56] J. Sodtipinta, C. Ieosakulrat, N. Poonyayant, P. Kidkhunthod, N. Chanlek, T. Amornsakchai, P. Pakawatpanurut, Interconnected open-channel carbon nanosheets derived from pineapple leaf fiber as a sustainable active material for supercapacitors, Ind. Crop. Prod. 104 (2017) 13–20, https://doi.org/10.1016/j.indcrop.2017.04.015.
[57] S. Yu, H. Wang, C. Hu, Q. Zhu, N. Qiao, B. Xu, Facile synthesis of nitrogen-doped, hierarchical porous carbons with a high surface area: the activation effect of a nano-ZnO template, J. Mater. Chem. A 4 (2016) 16341–16348, https://doi.org/10.1039/c6ta07047g.
[58] K. Ariga, A. Vinu, Y. Yamauchi, Q. Ji, J.P. Hill, Nanoarchitectonics for mesoporous materials, Bull. Chem. Soc. Jpn. 85 (2012) 1–32, https://doi.org/10.1246/bcsj.20110162.
[59] H. Kristianto, C.D. Putra, A.A. Arie, M. Halim, J.K. Lee, Synthesis and characterization of carbon nanospheres using cooking palm oil as natural precursors onto activated carbon support, Proc. Chem. 16 (2015) 328–333, https://doi.org/10.1016/j.proche.2015.12.060.
[60] A. Chandrasekaran, C. Patra, S. Narayanasamy, S. Subbiah, Adsorptive removal of ciprofloxacin and amoxicillin from single and binary aqueous systems using acid-activated carbon from Prosopis juliflora, Environ. Res. 188 (2020), 109825, https://doi.org/10.1016/j.envres.2020.109825.
[61] N. Gopal, M. Asaithambi, P. Sivakumar, V. Sivakumar, Adsorption studies of a direct dye using polyaniline coated activated carbon prepared from Prosopis juliflora, J. Water Process Eng. 2 (2014) 87–95, https://doi.org/10.1016/j.jwpe.2014.05.008.
[62] D.D. Zhou, H.J. Liu, Y.G. Wang, C.X. Wang, Y.Y. Xia, Ordered mesoporous/microporous carbon sphere arrays derived from chlorination of mesoporous TiC/C composite and their application for supercapacitors, J. Mater. Chem. 22 (2012) 1937–1943, https://doi.org/10.1039/c1jm14334d.
[63] S. Shanmugapriya, S. Surendran, Y.S. Lee, R.K. Selvan, Improved surface charge storage properties of Prosopis juliflora (pods) derived onion–like porous carbon through redox-mediated reactions for electric double layer capacitors, Appl. Surf. Sci. 492 (2019) 896–908, https://doi.org/10.1016/j.apsusc.2019.06.147.
[64] K. Krishnamoorthy, G.S. Kim, S.J. Kim, Graphene nanosheets: ultrasound assisted synthesis and characterization, Ultrason. Sonochem. 20 (2013) 644–649, https://doi.org/10.1016/j.ultsonch.2012.09.007.
[65] Y.J. Oh, J.J. Yoo, Y. Il Kim, J.K. Yoon, H.N. Yoon, J.H. Kim, S. Bin Park, Oxygen functional groups and electrochemical capacitive behavior of incompletely reduced graphene oxides as a thin-film electrode of supercapacitor, Electrochim. Acta 116 (2014) 118–128, https://doi.org/10.1016/j.electacta.2013.11.040.
[66] X. Huang, Q. Wang, X.Y. Chen, Z.J. Zhang, N-doped nanoporous carbons for the supercapacitor application by the template carbonization of glucose: the systematic comparison of different nitridation agents, J. Electroanal. Chem. 748 (2015) 23–33, https://doi.org/10.1016/j.jelechem.2015.04.024.
[67] G. Milczarek, A. Ciszewski, I. Stepniak, Oxygen-doped activated carbon fiber cloth as electrode material for electrochemical capacitor, J. Power Sources 196 (2011) 7882–7885, https://doi.org/10.1016/j.jpowsour.2011.04.046.
[68] T. Adinaveen, J.J. Vijaya, L.J. Kennedy, Comparative study of electrical conductivity on activated carbons prepared from various cellulose materials, Arab. J. Sci. Eng. 41 (2016) 55–65, https://doi.org/10.1007/s13369-014-1516-6.
[69] A. Barroso Bogeat, Understanding and tuning the electrical conductivity of activated carbon: a state-of-the-art review, Crit. Rev. Solid State Mater. Sci. 46 (2021) 1–37, https://doi.org/10.1080/10408436.2019.1671800.
[70] T. Adinaveen, L.J. Kennedy, J.J. Vijaya, G. Sekaran, Studies on structural, morphological, electrical and electrochemical properties of activated carbon prepared from sugarcane bagasse, J. Ind. Eng. Chem. 19 (2013) 1470–1476, https://doi.org/10.1016/j.jiec.2013.01.010.
[71] R.M. Bhattarai, K. Chhetri, S. Natarajan, S. Saud, S.J. Kim, Y.S. Mok, Activated carbon derived from cherry flower biowaste with a self-doped heteroatom and large specific surface area for supercapacitor and sodium-ion battery applications, Chemosphere. 303 (2022), 135290, https://doi.org/10.1016/j.chemosphere.2022.135290.
[72] Y. Sim, S. Surendran, H. Cha, H. Choi, M. Je, S. Yoo, D. Chan Seok, Y. Ho Jung, C. Jeon, D. Jin Kim, M.K. Han, H. Choi, U. Sim, J. Moon, Fluorine-doped graphene oxide prepared by direct plasma treatment for supercapacitor application, Chem. Eng. J. 428 (2022), 132086, https://doi.org/10.1016/j.cej.2021.132086.
[73] G. Zhang, Y. Chen, Y. Chen, H. Guo, Activated biomass carbon made from bamboo as electrode material for supercapacitors, Mater. Res. Bull. 102 (2018) 391–398, https://doi.org/10.1016/j.materresbull.2018.03.006.
[74] R. Bi, S.K. Pang, K.C. Yung, L.K. Yin, Comprehensive study of used cigarette filters-derived porous activated carbon for supercapacitors: from biomass waste to sustainable energy source, J. Electroanal. Chem. 925 (2022), 116915, https://doi.org/10.1016/j.jelechem.2022.116915.
[75] Y.C. Chen, L.Y. Lin, Investigating the redox behavior of activated carbon supercapacitors with hydroquinone and p-phenylenediamine dual redox additives in the electrolyte, J. Colloid Interface Sci. 537 (2019) 295–305, https://doi.org/10.1016/j.jcis.2018.11.026.
[76] R. Farma, Y. Tania, I. Apriyani, Conversion of hazelnut seed shell biomass into porous activated carbon with KOH and $CO_2$ activation for supercapacitors, Mater. Today Proc. (2023) 0–5, https://doi.org/10.1016/j.matpr.2023.02.099.
[77] H. Rustamaji, T. Prakoso, H. Devianto, P. Widiatmoko, K.A. Kurnia, Facile synthesis of N, S-modified activated carbon from biomass residue for promising supercapacitor electrode applications, Bioresour. Technol. Rep. 21 (2023) 101301, https://doi.org/10.1016/j.biteb.2022.101301.
[78] R. Farma, M. Deraman, A. Awitdrus, I.A. Talib, E. Taer, N.H. Basri, J. G. Manjunatha, M.M. Ishak, B.N.M. Dollah, S.A. Hashmi, Preparation of highly porous binderless activated carbon electrodes from fibres of oil palm empty fruit bunches for application in supercapacitors, Bioresour. Technol. 132 (2013) 254–261, https://doi.org/10.1016/j.biortech.2013.01.044.
[79] J. Devarajan, P. Arumugam, Boron-doped activated carbon from the stems of Prosopis juliflora as an effective electrode material in symmetric supercapacitors,

J. Mater. Sci. Mater. Electron. 33 (2022) 17469–17482, https://doi.org/10.1007/s10854-022-08595-x.

[80] Z. Peng, Z. Guo, W. Chu, M. Wei, Facile synthesis of high-surface-area activated carbon from coal for supercapacitors and high $CO_2$ sorption, RSC Adv. 6 (2016) 42019–42028, https://doi.org/10.1039/c5ra26044b.

[81] D. Dong, Y. Zhang, Y. Xiao, T. Wang, J. Wang, C.E. Romero, W. ping Pan, High performance aqueous supercapacitor based on nitrogen-doped coal-based activated carbon electrode materials, J. Colloid Interface Sci. 580 (2020) 77–87, https://doi.org/10.1016/j.jcis.2020.07.018.